ÓPTICA PURA Y APLICADA
www.sedoptica.es

Type: RESEARCH PAPER
Section: OPTOELECTRONICS

Investigation of Thermal Variations on Side Mode Suppression Ratio in the Dual Mode Spectroscopic Sensors

Investigación de las variaciones térmicas en la relación de supresión del modo lateral en los sensores espectroscópicos de modo dual

Usman Masud[1*], Abdul Razzaq Farooqi[2], M.S. Al-Buriahi[3], Talal M. Althagafi[4], Norah Salem Alsaiari[5]

1. PIMSAT, 74600, Karachi, Pakistan

2. Department of Electronic Engineering, Baghdad-ul-Jadeed Campus, The Islamia University of Bahawalpur, Pakistan

3. Department of Physics, Sakarya University, Sakarya, Turkey

4. Department of physics, college of science, Taif University, Taif 21944, Saudi Arbia

5. Department of Chemistry, College of Science, Princess Nourah bint Abdulrahman University, P.O. Box 84428, Riyadh 11671, Saudi Arabia

(*) E-mail: usmanmasud123@hotmail.com S: miembro de SEDOPTICA / SEDOPTICA member

Received: 22/9/2025 Accepted: 9/12/2025
DOI: 10.7149/OPA.58.4.51226

ABSTRACT:

A dual-mode biomedical sensor is being developed based on the principle of intra-cavity absorption spectroscopy. As the foundation of this system lies in Fibre Bragg Gratings, it is essential to thoroughly evaluate their complete performance following intense hysteresis analysis. Since two wavelengths (modes) are present in the system, we use the Side Mode Suppression Ratio to check their existence in the presence of neighboring ones, starting with an investigation at the specified temperature and injection current. Both modes have shown intense competition with the side modes, technically validated by two equipment. This revealed a novel correlation between the dominant modes and the side modes, considering numerous factors in cavity optomechanics, such as red and blue shifts. A strong interplay between different types of semiconductors in a lasing system is explored and established, which helps in understanding the development of our dual-mode sensor and discovering strong clues for the competition between multiple modes.

Keywords: Biomedical Sensor, Temperature-Dependent Sensor Behavior, Intracavity Absorption Spectroscopy, Fibre Bragg Grating, Dual Mode Laser, Side Mode Suppression Ratio, Cavity Optomechanics.

REFERENCES AND LINKS / REFERENCIAS Y ENLACE

[1] P. Sukul, J. K. Schubert, K. Zanaty, P. Trefz, A. Sinha, S. Kamysek, W. Miekisch, "Exhaled breath compositions under varying respiratory rhythms reflects ventilatory variations: translating breathomics towards respiratory medicine," Sci. Rep. **10**, 14109 (2020).

[2] O. Lawal, W. M. Ahmed, T. M. E. Nijsen, R. Goodacre, S. J. Fowler, "Exhaled breath analysis: a review of 'breath-taking' methods for off-line analysis," Metabolomics **13**, 110 (2017).

[3] D. I. Loaiza-Toscuento, D. Vazquez-Dominguez, A. P. Texis-Espinosa, J. C. Ramírez-San-Juan, R. Ramos-Garcia, T. Spezzia-Mazzocco, "The Impact of Methylene Blue in Antimicrobial Photodynamic Therapy Against Different Candida Species and Its Synergy with Fluconazole," Opt. Pura Apl. **57**(1) 51159 (2024).

[4] T. A. Popov, "Human exhaled breath analysis," Ann. Allergy Asthma Immunol. **106**(6), 451-456 (2011).

[5] J. Herbig, M. Muller, S. Schallhart, T. Titzmann, M. Graus, A. Hansel, "On-line breath analysis with PTR-TOF," J. Breath Res. **3**(2), 027004 (2009).

[6] U. Masud, "Investigations on highly sensitive optical semiconductor laser based sensorics for medical and environmental applications: The nanonose," Kassel University Press (2014).

[7] M. Phillips, R. N. Cataneo, C. Saunders, P. Hope, P. Schmitt, J. Wai, "Volatile biomarkers in the breath of women with breast cancer," J. Breath Res. **4**(2), 026003 (2010).

[8] W. Miekisch, J. K. Schubert, G. F. E. Noeldge-Schomburg, "Diagnostic potential of breath analysis - focus on volatile organic compounds," Clinica Chimica Acta, **347**(1-2), 25-39 (2004).

[9] K. M. Hangos, J. Bokor, G. Szederknyi, "Analysis and control of nonlinear process systems," Springer London (2004).

[10] M. Kaloumenou, E. Skotadis, N. Lagopati, E. Efstathopoulos, D. Tsoukalas, "Breath Analysis: A Promising Tool for Disease Diagnosis - The Role of Sensors," Sensors **22**(3), 1238 (2022).

[11] HSA Grants Provisional Authorisation for 'BreFence Go COVID-19 Breath Test System' and 'Traciex Breathalyser' for Detection of COVID-19 Infection. Available online: https://www.hsa.gov.sg/announcements/regulatory-updates/hsa-grants-provisional-authorisation-for-brefence-go-covid-19-breath-test-system-and-traciex-breathalyser-for-detection-of-covid-19-infection (accessed on 12 December 2025).

[12] M. Melgosa, F. J. Rodríguez-Pulido, L. Gómez-Robledo, M. Tejada-Casado, R. Bermejo, M. A. Murillo, F. J. Heredia, "Instrumental color measurements of automotive samples with convex cylindrical curvatures under diffuse lighting," Opt. Pura Apl. **57**(1), 51166 (2024).

[13] F. Güder, A. Ainla, J. Redston, B. Mosadegh, A. Glavan, T. J. Martin, G. M. Whitesides, "Paper-Based Electrical Respiration Sensor," Angew. Chem. Int. Ed. Engl. **55**, 5727-5732 (2016).

[14] V. M. Baev, J. Eschner, E. Paeth, "Intra-cavity spectroscopy with diode lasers," Appl. Phys. B **55**, 463-477 (1992).

[15] U. Masud, F. Jeribi, A. Zeeshan, A. Tahir, M. Ali, "Highly sensitive microsensor based on absorption spectroscopy: Design considerations for optical receiver," IEEE Access **8**, 100212-100225 (2020).

[16] V. M. Baev and P. E. Toschek, "Sensitivity limits of laser intracavity spectroscopy," Proc. SPIE 1715, Optical Methods in Atmospheric Chemistry, 381-392 (1993).

[17] A. Champagne, M. Lestrade, J. Camel, R. Maciejko and B. Tromborg, "Degradation of side-mode suppression ratio in a DFB laser integrated with a semiconductor optical amplifier," IEEE J. Quantum Electron. **40**(7), 871-877 (2004).

[18] A. Einstein, "Grundgedanken der allgemeinen Relativitätstheorie und Anwendung dieser Theorie in der Astronomie," Preuß. Akad. der Wissenschaften, Sitzungsberichte **315**, 778-786 (1915).

[19] A. J. Ward, D. J. Robins, G. Busico, E. Barton, L. Ponnampalam, J. P. Duck, N. D. Whitbread, P. J. Williams, D. C. J. Reid, A. C. Carter, M. J. Wale, "Widely tunable DS-DBR laser with monolithically integrated SOA: design and performance," IEEE J. Sel. Top. Quantum Electron. **11**(1), 149-156 (2005).

[20] Y. Posudin, "Methods of Analysis of Volatile Organic Compounds," in Methods of Measuring Environmental Parameters, John Wiley & Sons (2014).

[21] W. Demtröder, "Experimentalphysik 3: Atome, Moleküle und Festkörper (Springer-Lehrbuch)," Berlin, Heidelberg: Springer Berlin Heidelberg, (2005).

[22] B. Van Zeghbroeck, "Principles of Semiconductor Devices," University of Colorado (2007).

[23] U. Masud, M. R. Amirzada, H. Elahi, F. Akram, A. Zeeshan, Y. Khan, M. K. Ehsan, M. A. Qureshi, A. Ali, S. Nawaz, U. Ghafoor, "Design of two-mode spectroscopic sensor for biomedical applications: analysis and measurement of relative intensity noise through control mechanism," Appl. Sci. **12**(4), 1856 (2022).

[24] U. Masud and M. I. Baig, "Investigation of cavity length and mode spacing effects in dual-mode sensor," IEEE Sens. J. **18**(7), 2737-2743 (2018).

[25] J. C. Atenco-Cuautle, N. Perez-Perez, M. G. Delgado-Lopez, J. Ramirez-Ramirez, J. C. Ramirez-San-Juan, R. Ramos-Garcia, T. Spezzia-Mazzocco, "Photodynamic therapy with non-porphyrin photosensitizers in breast cancer and non-cancer cells," Opt. Pura Apl. **57**(1), 51161 (2024).

[26] N. Meinzer, "One mode at a time," Nat. Phys. **17**, 987 (2021).

[27] U. Masud, M. Ali, F. Qamar, A. Zeeshan, M. Ikram, "Dual mode spectroscopic biomedical sensor: Technical considerations for the wireless testbed," Phys. Scr. **95**, 105206 (2020).

[28] Z. Gao, L. Wang, Jian-Jun He, "Mode competition analysis in dual-wavelength coupled-cavity semiconductor laser," J. Opt. Soc. Am. B **27**, 432-441 (2010).

[29] U. Masud, M. I. Baig, "Development of an Optical Sensor for the Detection of Volatile Organic Compounds," 2011 Frontiers of Information Technology, Islamabad, Pakistan, 321-326 (2011).

[30] U. Masud, M. I. Baig, "Multimode Competition in Lasers in the Light of Optical Feedback," 10th International Conference on Frontiers of Information Technology, Islamabad, Pakistan, 243-247 (2012).

[31] U. Masud, M. Ali, F. Qamar, A. Zeeshan, M. Ikram, "Dual mode spectroscopic biomedical sensor: Technical considerations for the wireless testbed," Phys. Scr. **95**, 105206 (2020).

[32] A. Martínez-García, J. A. Rayas-Alvarez, C. Meneses-Fabián, S. Mansurova, P. Segovia-Olvera, "SEDOPTICA Editorial Optics and Photonics in Mexico," Opt. Pura Apl. **58**(1) 5811 (2025).

[33] M. Delgado, B. Santamaría, M. B. Tomás, "Woman in Optics and Photonics committee's report," Opt. Pura Apl. **58**(3) 5833 (2025).

[34] F. W. Wise, A. Chong, W. H. Renninger, "High-energy femtosecond fiber lasers based on pulse propagation at normal dispersion," Laser Photon Rev. **2**, 58-73 (2008).

[35] S. Valentin, J. Shrestha, private communication.

[36] L. Yu-Lung, C. Han-Sheng, "Measurement of thermal expansion coefficients using an in-fibre Bragg-grating sensor," Measurement Science and Technology **9**(9), 1543-1547 (1998).

[37] Inphenix Semiconductor Optical Amplifier, Inphenix, Inc., USA, https://www.inphenix.com/semiconductor-optical-amplifier/ (visited on December 12, 2025).

[38] LDC-3900 ILX Lightwave Laser Diode Controller, https://www.newport.com/p/LDC-3900-120V (accessed on 12 December 2025).

[39] Advanced Optics Solutions GmbH, Overbeckstr 39a, D-01139 Dresden, https://www.aos-fiber.com/eng/Company.html (accessed on 12 December 2025).

[40] The Rohde & Schwarz signal and spectrum analyser portfolio, https://www.rohde-schwarz.com/products/test-and-measurement/signal-and-spectrum-analyzers_63665.html (accessed on 12 December 2025).

[41] Tektronix electrical spectrum analyzer, https://www.tek.com/en/products/spectrum-analyzers (accessed on 12 December 2025).

[42] Teledyne LeCroy WaveRunner 9000 oscilloscope, https://www.teledynelecroy.com/wr9000/ (accessed on 12 December 2025).

[43] C. Elliott, V. Vijayakumar, W. Zink, R. Hansen, "National Instruments LabVIEW: A Programming Environment for Laboratory Automation and Measurement," SLAS Technol. **12**(1), 17-24 (2007).

[44] U. Masud, A. R. Farooqi, M. Kashif, "Investigation of nonlinear optical effects with fibre Bragg gratings and signal-to-noise ratio in the evolution of highly sensitive system," Eur. Phys. J. D **78**, 42 (2024).

[45] OptiSplice M90e Fusion Splicer - Corning, https://docs.msp-ict.com/corning-fusion-splicer-M90E-0SM-T-H-en.html (accessed on 12 December 2025).

[46] H. Angus MacLeod, Thin-Film Optical Filters, Third Edition (Series in Optics and Optoelectronics), CRC Press (2001).

[47] K. P. Chen, P. R. Herman, R. Tam, "Strong fiber Bragg grating fabrication by hybrid 157- and 248-nm laser exposure," IEEE Photonics Technol. Lett. **14**(2), 170-172, (2002).

[48] S. J. Mihailov, D. Grobnic, Huimin Ding, C. W. Smelser, J. Broeng, "Femtosecond IR laser fabrication of Bragg gratings in photonic crystal fibers and tapers," IEEE Photonics Technol. Lett. **18**, 1837-1839 (2006).

[49] C. S. Goh, S. Y. Set, K. Kikuchi, "Design and fabrication of a tunable dispersion-slope compensating module based on strain-chirped fiber Bragg gratings," IEEE Photonics Technol. Lett. **16**(2), 524-526 (2004).

[50] H. Bartelt, K. Schuster, S. Unger, C. Chojetzki, M. Rothhardt, I. Latka, "Single-pulse fiber Bragg gratings and specific coatings for use at elevated temperatures," Appl. Opt. **46**(17), 3417-3424 (2007).

[51] A. Othonos, "Fiber Bragg gratings," Rev. Sci. Instrum. **68**, 4309-4341 (1997).

[52] W. Alayed, M. Ikram, U. Masud, "Preparation of dual mode spectroscopic system for testing: Analysis of sample holder and investigation of intensity noise," Heliyon **11** (3), e42294 (2025).

[53] C. Almaguer-Gómez, J. F. Almaguer-Medina, G. Chávez-Aquino, V. M. Chávez-Pérez, A. G. Cruz-Sánchez, L. H. González-Villegas, "Astronomical Observation in Mexico Transitioning from the Visible to the Invisible: A Brief Historical Overview," Opt. Pura Apl. **58**(1) 51200 (2025).

[54] A. Gearba, G. Cone, "Numerical analysis of laser mode competition and stability," Physics Letters A **269** (2-3), 112-119 (2000).

[55] B. Peng, Ş. K. Özdemir, S. Rotter, H. Yilmaz, M. Liertzer, F. Monifi, C. M. Bender, F. Nori, L. Yang, "Loss-induced suppression and revival of lasing," Science **346**, 328-332 (2014).

[56] S. Bittner, S. Guazzotti, Y. Zeng, X. Hu, H. Yilmaz, K. Kim, S. S. Oh, Q. J. Wang, O. Hess, H. Cao, "Suppressing spatiotemporal lasing instabilities with wave-chaotic microcavities," Science **361**, 1225-1231 (2018).

[57] M. Lewenstein, M. F. Ciappina, E. Pisanty, J. Rivera-Dean, P. Stammer, Th. Lamprou, P. Tzallas, "Generation of optical Schrodinger cat states in intense laser-matter interactions," Nat. Phys. **17**, 1104-1108 (2021).

[58] R. Chriki, E. Maguid, C. Tradonsky, V. Kleiner, A. A. Friesem, N. Davidson, E. Hasman, "Spin-controlled twisted laser beams: intra-cavity multi-tasking geometric phase metasurfaces," Opt. Express **26**, 905-916 (2018).

[59] S. Martinez, S. C. Dulebohn, "Patient Education: Anesthesia," Treasure Island (FL): StatPearls Publishing; (2024) https://www.ncbi.nlm.nih.gov/books/NBK606110/ (accessed on 12 December 2025).

[60] American Society of Anesthesiologists, Anesthesia 101 (https://www.asahq.org/whensecondscount/anesthesia-101/) (accessed on 12 December 2025).

[61] P. Schober, T. R. Vetter, "Systematic Review in Clinical Research," Anesthesia & Analgesia **131**(3), 762-763 (2020).

[62] National Institute of General Medical Sciences (U.S.), Anesthesia (https://www.nigms.nih.gov/education/fact-sheets/Pages/anesthesia.aspx) (accessed on 12 December 2025).

[63] R. D. Miller, "Landmark Papers in Anaesthesia," Anesthesiology **122**(2), 475-476 (2015).

[64] M. Jahangiri, F. Moradiani, G. M. Parsanasab, M. Mirmohammadi, "High side-mode suppression ratio with a Vernier effect single-mode laser using triple coupled microrings," Sci. Rep. **13**, 7092 (2023).

[65] K. Ospino-Manjarres, D. Zambrano-Gutierrez, J. M. Cruz-Duarte, D. Jauregui-Vazquez, C. E. Osornio-Martinez, J. G. Avina-Cervantes, K. Escalante-Sanchez, R. Rojas-Laguna, "Study of machine learning techniques for robotic finger monitoring using image based macro-bending fiber optic sensor," Opt. Pura Apl. **58**(1), 51187 (2025).

[66] Long Wavelength Optical Spectrum Analyzer AQ6375, https://tmi.yokogawa.com/solutions/discontinued/aq6375-optical-spectrum-analyzer/ (accessed on 12 December 2025).

[67] P. E. Toschek, V. M. Baev, "One Is Not Enough: Intra-Cavity Spectroscopy with Multi-Mode Lasers," in Lasers, Spectroscopy and New Ideas. Springer Series in Optical Sciences, vol. 54. Springer, Berlin, Heidelberg (1987).

[68] G. A. Reider, "Photonik: Eine Einführung in die Grundlagen," 2. Auflage. Wien: Springer-Verlag, (2005).

[69] Thorlabs OSA202 - Fourier Transform Optical Spectrum Analyzer, 600 – 1700 nm, https://www.thorlabs.com/thorproduct.cfm?partnumber=OSA202 (accessed on 12 December 2025).

[70] Optical Spectrum Analysis, Application Notes, https://www.keysight.com/us/en/assets/3120-1501/application-notes/5963-7145.pdf (accessed on 12 December 2025).

[71] R. Paschotta, Optical Spectrum Analyzers, https://www.rp-photonics.com/optical_spectrum_analyzers.html (accessed on 12 December 2025).

[72] K. Schmidt, I. Podmore, "Current challenges in volatile organic compounds analysis as potential biomarkers of cancer," J. Biomark. **2015**(1), 981458 (2015).

[73] R. Epping, M. Koch, "On-site detection of volatile organic compounds (VOCs)," Molecules **28**(4), 1598 (2023).

[74] Technical meetings with the Anaesthesiology and Health Promotion Departments, Railway General Hospital, Westridge Rawalpindi.

[75] A. Imada, T. Mukai, A. Fujiwara, H. J. Lee, S. Hasegawa, H. Asahi, "Reduced temperature dependence of refractive index in TlInGaAs by addition of T1," 16th IEEE International Conference on Indium Phosphide and Related Materials, 465-468 (2004).

[76] L. K. Sørensen, D. E. Khrennikov, V. S. Gerasimov, A. E. Ershov, S. P. Polyutov, S. V. Karpov, H. Agren, "Nature of the anomalous size dependence of resonance red shifts in ultrafine plasmonic nanoparticles," J. Phys. Chem. C **126**(39), 16804-16814 (2022).

[77] X. Liu, J. Liu, B. Liang, Y. Wang, Y. Guo, C. Wang, S. Wang, G. Fu, Yuriy I. Mazur, Y. Maidaniuk, M. E. Ware, G. J. Salamo, "Type-II characteristics of photoluminescence from InGaAs/GaAs surface quantum dots due to Fermi level pinning effect," Appl. Surf. Sci. **578**, 152066 (2022).

[78] E. J. Skogen, L. A. Coldren, J. W. Raring, S. P. DenBaars, "Multiple-band-edge quantum-well intermixing in the InGaAs/InGaAsP/InGaP material system," Appl. Phys. Lett. **86**, 241117 (2005).

[79] Chapter 2 - Refractive Index, Editor(s): Edward D. Palik, Handbook of Optical Constants of Solids, Academic Press, 5-114, (1997).

[80] J. Sun, J. Lin, M. Zhou, J. Zhang, H. Liu, T. You, X. Ou, "High-power, electrically-driven continuous-wave 1.55-µm Si-based multi-quantum well lasers with a wide operating temperature range grown on wafer-scale InP-on-Si (100) heterogeneous substrate," Light Sci. Appl. **13**, 71 (2024).

[81] Y. Wang, H. Wu, C. Chen, Y. Zhou, Y. Wang, L. Liang, Z. Tian, L. Qin, L. L. Wang, "An ultra-high-SMSR external-cavity diode laser with a wide tunable range around 1550 nm," Appl. Sci. **9** (20), 4390 (2019).

[82] A. T. T. Pham, O. K. T. Le, D. V. Hoang, T. H. Nguyen, K. H. Chen, S. Park, T. B. Phan, V. C. Tran, "Coupling modification of Fermi level, band flattening and lattice defects to approach outstanding thermoelectric performance of ZnO films via tuning In and Ga incorporation," Acta Mater. **241**, 118415 (2022).

[83] D. M. Shemwell, K. E. Robinson, R. I. Gellert, D. C. Quimby, J. Ross, J. M. Slater, A. A. Vetter, J. Zumdieck, "Optical cavities for visible free-electron laser experiments," Nuclear Instruments and Methods in Physics Research - Section A (NIM-A) **259**, 56-61 (1987).

[84] U. Masud, M. I. Baig, A. Zeeshan, "Automatization analysis of the extremely sensitive laser-based dual-mode biomedical sensor," Lasers Med. Sci. **35**, 1531-1542 (2020).

[85] M. Cardona, P.Y. Yu, "Optical Properties of Semiconductors," in Comprehensive Semiconductor Science and Technology, Elsevier, 125-195 (2011).

[86] K. Aoki, T. Kawaguchi, K. Ohta, "The Largest Blueshifts of [O III] emission line in two narrow-line quasars," The Astrophysical Journal **618**, 601-608 (2005).

[87] Britannica, The Editors of Encyclopaedia. "Fermi level". Encyclopedia Britannica, 6 Oct. 2006, https://www.britannica.com/science/Fermi-level (accessed on 12 December 2025).

[88] S. W. Boettcher, S. Z. Oener, M. C. Lonergan, Y. Surendranath, S. Ardo, C. Brozek, P. A. Kempler, "Potentially Confusing: Potentials in Electrochemistry," ACS Energy Lett. **6**(1), 261-266 (2021).

1. Introduction

One of the emerging areas of research in the current world involves analyzing the gases that are exhaled in human breath to detect drugs [1–3]. This is done to monitor, identify, and treat signs of illness in individuals by examining the levels of substances that influence the composition of respiratory gas. This helps in the detection of potential diseases or drug doses in individuals, based on this information. These substances, which enter the bloodstream, are referred to as Volatile Organic Compounds (VOCs) or biomarkers [4–7]. Although more than 500 different compounds have been identified as biomarkers in breath, but they are typically found in very small quantities.

To detect these low concentrations of VOCs, various analytical approaches are being actively explored and utilized, including, but not limited to, sophisticated techniques such as mass spectrometry and gas chromatography [8, 9]. These traditional methods, although widely used, exhibit certain limitations that can hinder their effectiveness in accurately identifying and quantifying VOCs. For instance, issues related to time resolution arise, resulting in delays that can complicate the resulting investigation. Additionally, these methods often have lower detection resolution, making it challenging to distinguish between related compounds. Additionally, detection ambiguity is another significant drawback, as the presence of other

VOCs can interfere with the results, leading to a misinterpretation of the data. Moreover, such traditional approaches may struggle with sensitivity, particularly when identifying VOCs present in extremely low concentrations [10–13].

In this context, an alternative and potentially advantageous option for detecting VOCs is the use of absorption spectroscopy [14–16]. This method involves passing light through a sample and analysing the interaction between the light and the molecules present in that sample. By observing how the light is absorbed across specific wavelengths, researchers can draw meaningful conclusions about the characteristic properties of the sample being examined. In its most straightforward explanation, the energy of the light interacts with the molecules, resulting in absorption at defined wavelength ranges. This phenomenon can be indicative of the presence and concentration of different VOCs [17–19]. This technique can offer significantly improved sensitivity and isolation, potentially overcoming some of the limitations associated with traditional VOC detection methods [20–22].

Our research focuses on the development of a laser-based experimental setup specifically designed for use as a biomedical sensor [15, 23, 24]. In our approach, we aim to utilize two distinct wavelengths instead of a single wavelength. This decision is based on the compelling reasons related to the enhanced sensitivity that dual-wavelength operation can provide for the system [6, 14, 16, 25–28]. By leveraging these two wavelengths, we can significantly improve the overall performance and effectiveness of the sensor, making it more suitable for various biomedical applications.

At the heart of our current work is a thorough and detailed investigation into the properties and behaviors of Fibre Bragg Gratings (FBGs), which are crucial components of our experimental setup. FBGs play a fundamental role in the operation of the sensor, as they can reflect specific wavelengths of light while allowing other wavelengths to pass through, providing a means to finely tune the sensor's response [32, 34–36].

To optimize the functioning of the FBGs within our system, we are delving into the phenomenon known as the Side Mode Suppression Ratio (SMSR) [17, 27, 33, 64]. The SMSR is an important parameter that quantifies the suppression of unwanted side modes relative to the main operational mode. By engaging in this envelopment, we aim to enhance the quality and precision of the sensor's output, thereby increasing its reliability and applicability in biomedical settings.

Ultimately, our work seeks to contribute to the advancement of biomedical sensing technologies by exploring innovative approaches that enhance sensitivity and performance through the strategic application of laser modes and the effective use of Fibre Bragg Gratings. Through this research, we hope to pave the way for the development of next-generation biomedical sensors that can provide reliable and accurate measurements in various medical and healthcare contexts.

2. Experimental Setup

The spectroscopic setup (Figure 1(a)) consists of light that is emitted by the laser assembly (Semiconductor Optical Amplifier (SOA), amplified by the loop mirror) [6, 14, 15, 37]. A Laser Diode Controller (LDC) controls the temperature and injection current of the SOA [38] that can be connected to a computer (Figure 1(b)). This light enters two FBGs, classified as FBG_i/FBG1 and FBG_o/FBG2, through optical couplers V_i and V_o, respectively [39]. This forms the basis of Intra-Cavity Absorption Spectroscopy (ICAS), which, in principle, generates two laser lines by placing the devices inside the laser cavity. As the SOA emits light in the Near Infrared, the FBGs are also designed to operate in the same wavelength domain (1538-1545 nm). Isolators ensure the propagation of light in one direction.

For the sake of measurement, an Optical Spectrum Analyser (OSA) is used in the system. This records the output spectrum of light at the required wavelengths [40–42]. For electrical measurement, this can be achieved by converting the optical output into an electrical equivalent using a Photodiode, bias t, and a low-noise amplifier. An Electrical Spectrum Analyser, Voltmeter and Oscilloscope are engaged to record the corresponding electrical signals. This system can be controlled by a computer via LabVIEW that assists in controlling the experimentation [23, 26, 43, 44].

2.a. Cavity Optomechanics

It is important to understand the mechanics of the system's operation in Figures 1(a) and 1(b) in light of the working FBGs, with particular attention to the former one. Light from the lasing system enters the FBGs via coupler V_i. It is reflected by the specific wavelength of the grating FBG_i, as per Bragg's theory. This light can be detected at the OSA after passing through Isolator I_2. The remaining portion is passed on to the coupler V_o and goes to FBG_o. Here, the light is reflected by the specific wavelength of the grating FBG_o and can be detected solely at OSA, passing through Isolator I_4. The remaining portion of the light is reflected back into the entire cavity of the system, at all wavelengths of the SOA. Therefore, we observe the formation of two main cavities in the system, each corresponding to a grating: the inner cavity (light reflected by FBGi) and the outer cavity (light reflected by FBG_o). The entire procedure is illustrated in Figure 2, which shows the formation of cavities in the system in Figure 1(a).

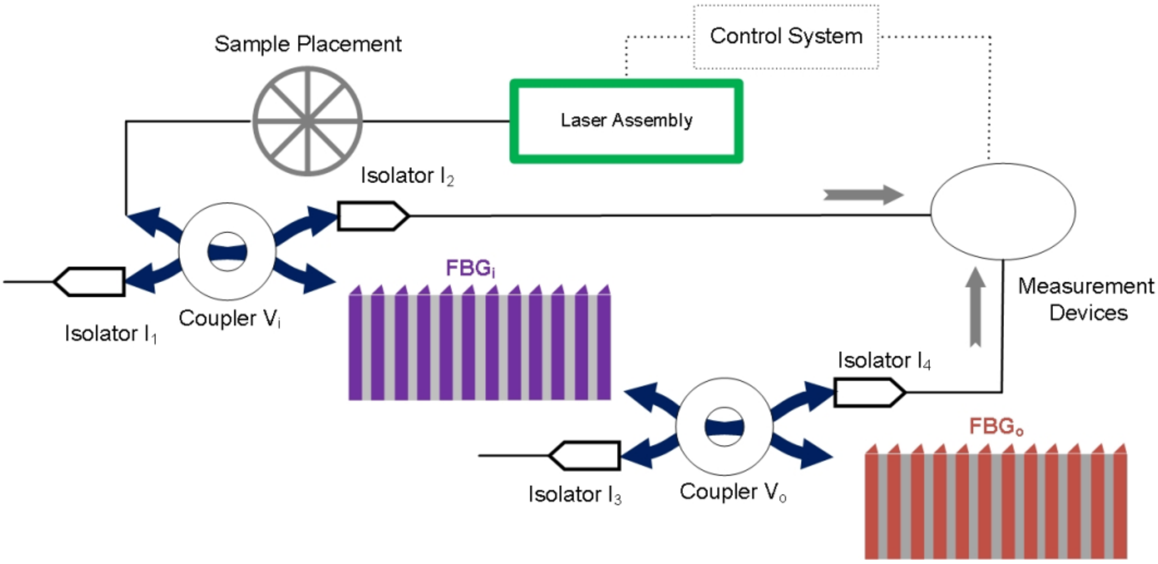

(a)

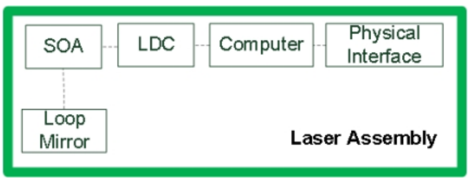

(b)

Fig. 1: (a) The measurement system containing the components, and (b) magnified view of the Laser Assembly, consisting of the SOA, Loop Mirror, LDC, and Physical Interface.

The colors of FBG_i and FBG_o have been retained in this figure. Figures 2(a) and 2(b) differentiate the cavities in the system that were made by these FBGs. Finally, Figure 2(c) shows the complete system cavity, which contains all the components. In this manner, the system operates on two specific wavelengths of the FBGs, which are present in the gain profile of the SOA, as illustrated in Figure 3. The intensity of both modes can be adjusted by allowing light to pass through them, via the couplers (V_i for FBG_i and V_o for FBG_o, respectively). The difference in intensity levels between these modes, tuned to the specific wavelength of the sample (VOC), and analysis of the absorption spectrum can provide a useful amount of information about the substance of interest, underpinning the idea behind the anticipated sensor. An idealized illustration of this output in the form of an absorption spectrum is shown in Figures 3(a) and 3(b).

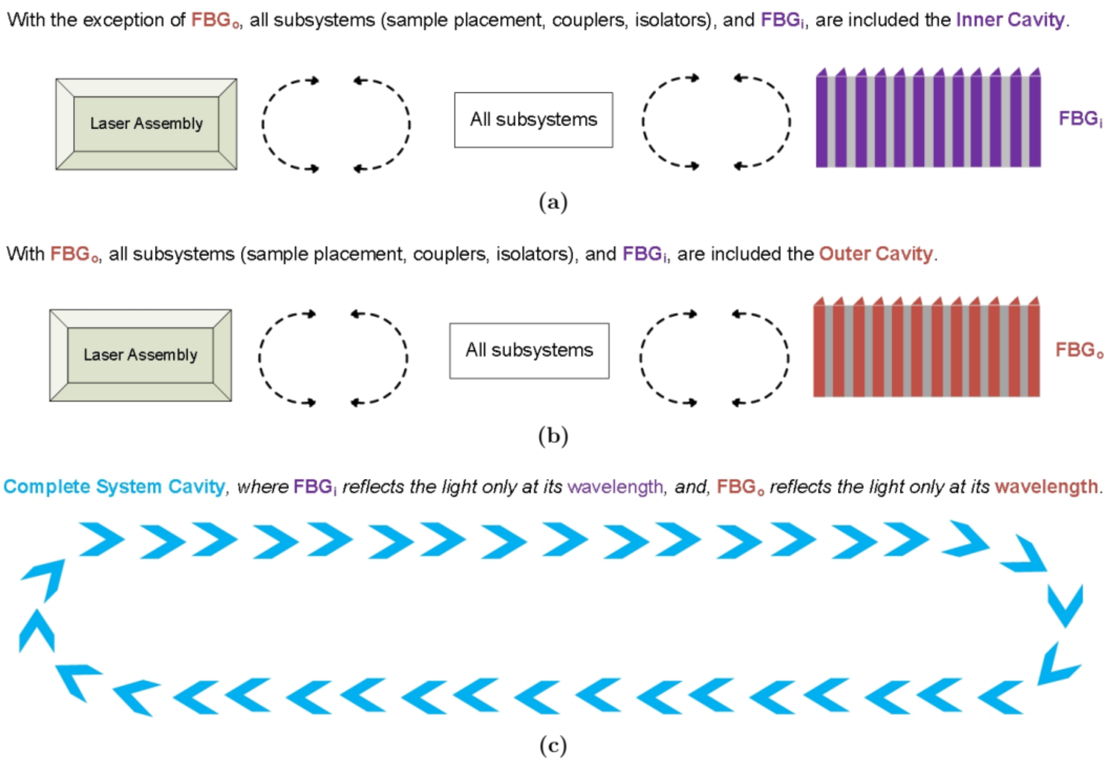

Fig. 2: An idealized illustration of the measurement system containing the components: FBGs and the difference in their roles in the measurement system. (a) and (b) show FBG_i and FBG_o, respectively, whereas (c) generalizes the complete system that contains both FBGs (FBG_i and FBG_o) in it.

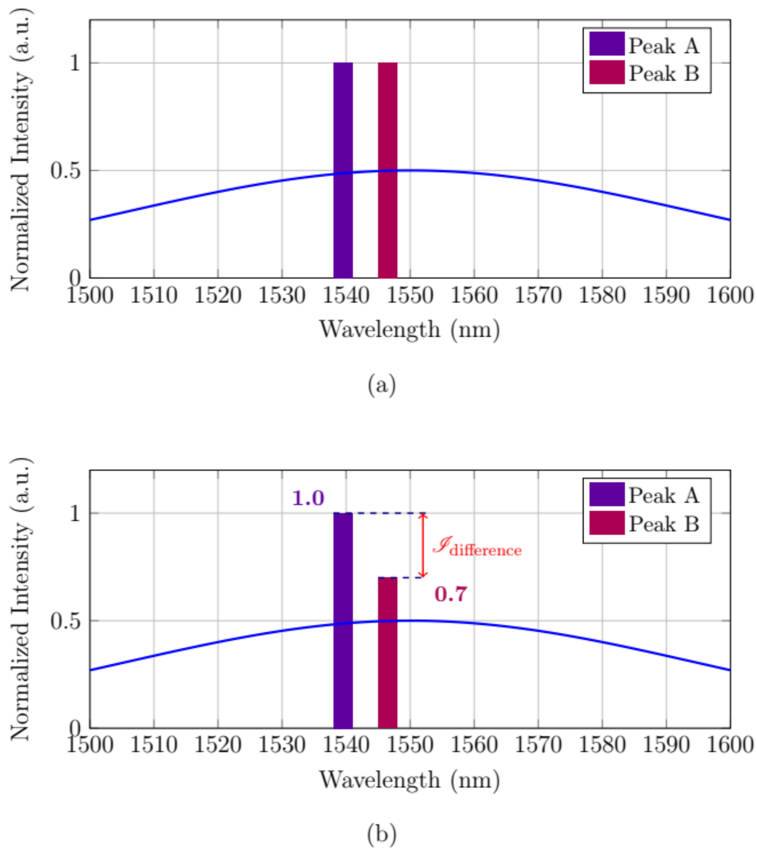

Fig. 3: Illustration of laser gain curve (in blue), with output from I4 in Figure 1, and highlighted regions for Peak A and Peak B, corresponding to FBG_i and FBG_o, respectively. The red arrow shows the difference in normalized intensity ($\mathscr{I}_{difference}$) between the two peaks. Dotted lines and colored labels highlight each peak's maximum intensity. (a) shows both modes at the same level, and (b) shows the modified gain response with their difference $\mathscr{I}_{difference}$ with the red arrows, (in conjunction with Figure 2).

2.b. Bridging Past Insights with Current and Future Work

Some of the relevant ones can be summarized in the flowchart in Figure 4.

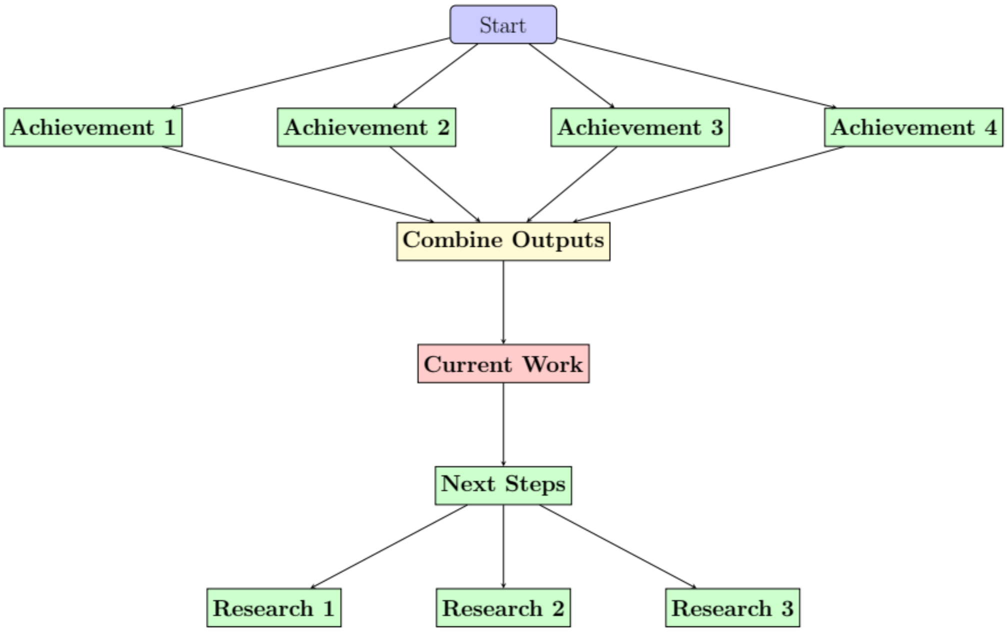

Fig. 4: Flowchart illustrating the correlation between some of the prior achievements and the current work, highlighting integration, progression, and future research directions.

Achievement 1: Some of the initial work on the topic was conducted in [6], which yielded interesting outcomes in various aspects, preceded by its modeling scheme [29, 30]. These opened numerous corridors.

Achievement 2: To understand cavity optomechanics, the entire system was analyzed with respect to intensity noise, a crucial parameter as discussed in [24].

Achievement 3: The next barrier was the design of the optical receiver, which successfully provided the necessary output, as reported in [15].

Achievement 4: To expedite the experimentation procedure, most of the devices were equipped with a control mechanism [23]. As the project is intended for a biomedical entity, efforts were focused on correlating it with wireless schemes [31].

Recent developments include, but are not limited to, worthwhile results on cavity lengths, intensity measurements (Research 1), temporal analysis, and sample measurements (Research 2) [6, 15, 23, 24, 44]. These breakthroughs in the field have sparked our interest in a new parameter: the SMSR. This parameter is becoming increasingly important for assessing the performance and efficiency of laser systems and holds pivotal importance in multimode laser sensors.

Investigation of SMSR (Research 3, current work) is anticipated to lead to various research themes, including intensity noise, temporal investigation, and measurements with relevant compounds. Before starting the measurements with SMSR, it is essential to check the losses that occur in the system due to the optical fibre, specifically the splice loss.

2.c. Splice Loss

It is mandatory to check the splice loss that occurs at each optical junction within the setup in Figure 1(a), before proceeding with measurements. For this purpose, we used the OptiSplice™ LID splicing device [45]. This advanced device is designed to automatically position fibres relative to each other before fusing them together. This automation not only ensures precision but also significantly increases the speed and efficiency of the splicing process.

With careful and meticulous work, the OptiSplice™ LID splicing device is capable of achieving remarkably low splicing losses. Typically, losses of 0 to 0.01 dB can be detected, which is a testament to the device's impressive capabilities. Furthermore, the measurement error is stated to be ±0.02 dB, indicating a high level of accuracy.

One of the standout features of this splicing device is its ability to monitor and assess the loss caused by the splice in real-time. By checking the losses as the splice is being made, this device enables users to maintain optimal performance and minimize potential issues. Thus, the optical connections (splices) were successfully made with its help, and the values of various splices are provided in Table 1, which are within the acceptable limits.

2.d. Fibre Bragg Gratings

FBGs enable tunable modes in the sensor to be developed, based on the principle of the grating structure of the Distributed Bragg Reflector (DBR) [46]. This device can be integrated directly into the fibre. In this case, the different refractive index is caused by a change in the glass fibre. Its refractive index can be changed by absorbing both UV laser light, as in [47], and IR laser light, as in [48]. According to [49], FBGs can be fabricated with a deformation that also has a chirped profile, allowing them to reflect multiple Bragg wavelengths. The reflectance of the FBGs can be more than 99.8% [50].

TABLE 1. Determination of the splice losses at various points in Figure 1(a).

No.	Splice Point	Value (dB)	Within Limit
1	Laser Assembly and Sample Placement	0.21	Yes
2	Sample Placement and V_i	0.24	Yes
3	V_i and I_1	0.22	Yes
4	V_i and I_2	0.25	Yes
5	V_i and FBG_i	0.25	Yes
6	FBG_i and V_o	0.23	Yes
7	V_o and FBG_o	0.24	Yes
8	V_o and I_3	0.21	Yes
9	V_o and I_4	0.22	Yes

For our purpose, only single-mode fibres are used. Single-mode in this context means that only the lowest order mode, also called fundamental mode, can be formed in the transverse and lateral directions. In single-mode fibres, the fibre core is so thin that higher-order transverse and lateral modes are not supported. In addition, the angle of incidence between the electromagnetic waves and the FBG in the glass fibre is almost 90°, which simplifies the Bragg condition equation

$$\lambda_B = 2 \cdot n_{eff} \Lambda. \tag{1}$$

Here, λ_B is the Bragg wavelength, n_{eff} is the effective refractive index, and Λ is the period of the grating. As highlighted above, only one mode is reflected in an FBG, and its Bragg wavelength can be calculated accordingly. This relationship enables the specification of a single wavelength within a broadband spectrum. In our system, we have two FBGs that reflect at their respective wavelengths within the SOA, enabling a dual-mode sensor [6, 39, 52]. For example, Figure 5 illustrates the reflection spectrum of an ideal FBG. The intensity is distributed over a narrow spectral line and is otherwise zero.

FBGs are highly sensitive to changes caused by mechanical stress or temperature fluctuations. According to [51], the following dependence of the Bragg wavelength of FBGs in relation to temperature and mechanical stress results:

$$\Delta\lambda_B = 2\left(\Lambda\frac{\partial n}{\partial l} + n\frac{\partial \Lambda}{\partial l}\right)\Delta l + 2\left(\Lambda\frac{\partial n}{\partial T} + n\frac{\partial \Lambda}{\partial T}\right)\Delta T. \tag{2}$$

The Bragg wavelength change $\Delta\lambda_B$ is determined from the partial derivatives of the effective refractive index and the grating period with respect to the length ∂l multiplied by its change Δl and the partial derivatives of ∂n and $\partial \Lambda$ with respect to the temperature T multiplied by its change ∂T. According to Equation 2, the change in the Bragg wavelength can be attributed to temperature changes and mechanical stresses, implying a detailed investigation of the FBGs in our system [6, 52].

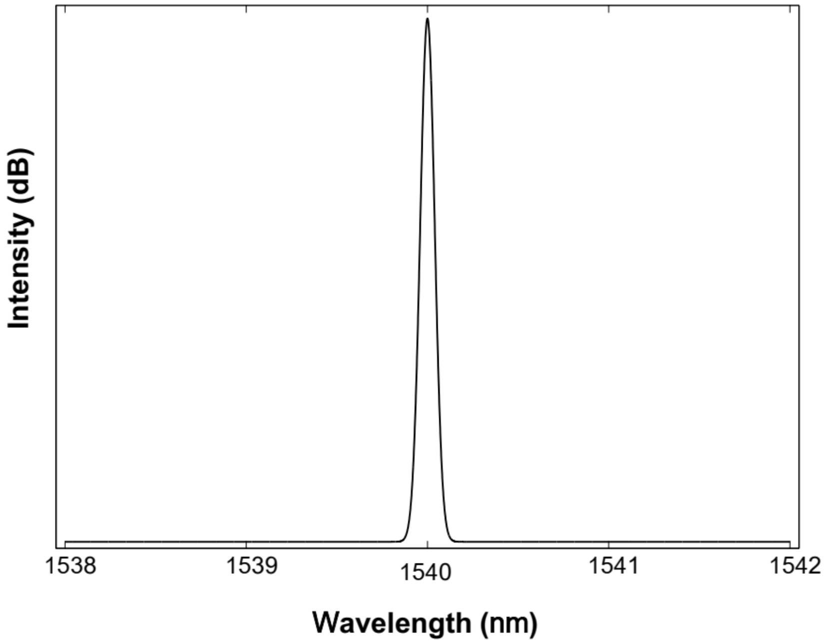

Fig. 5: Example of a spectrum of an FBG.

2.e. The Driving Forces of the Working Mechanism and Merits

The essence of our experimental work lies in the operation of both FBGs. Numerous wavelengths, or modes, exist in a laser system at any time [28, 53, 54]. When a multimode system is used, these modes compete with each other at all times. It is very difficult to analyze these modes at all times, due to technical and monetary limitations [55]. A single-mode laser is, on the contrary, better in terms of these constraints. However, this system limits sensitive operation and experimentation [56]. Therefore, we resort to a dual mode system that combines the benefits of both scenarios [16, 57, 58]. The plan is to develop a biomedical sensor setup that combines these features and can be used later to monitor the constituents of human breath exhaled from the lungs [6, 24]. This air will contain information about VOCs, which will help physicians determine the amount of anesthesia that must be administered to a particular patient. Medical science reveals that there is no strict regulation worldwide to provide a certain amount of anesthesia to a patient, and this opens up opportunities for work at present [59–63]. To the best of our knowledge, this is the only proposal that utilizes this mechanism, and some of the worthwhile results are presented in [6, 15, 23, 24, 44, 84].

In this work, we analyze an intense mode competition between the two wavelengths (modes) M_i and M_o under the effects of temperature and injection current. Since the laser system depends on these modes, it is important to understand their existence at various times. We measure the SMSR of both modes in the system under intense parametric conditions of temperature and injection current.

2.f. Side Mode Suppression Ratio (SMSR)

An important quantity used to characterize a laser is the SMSR [17, 27, 64]. The SMSR indicates the difference in intensity between the main oscillating mode and the next stronger side mode (Figure 6).

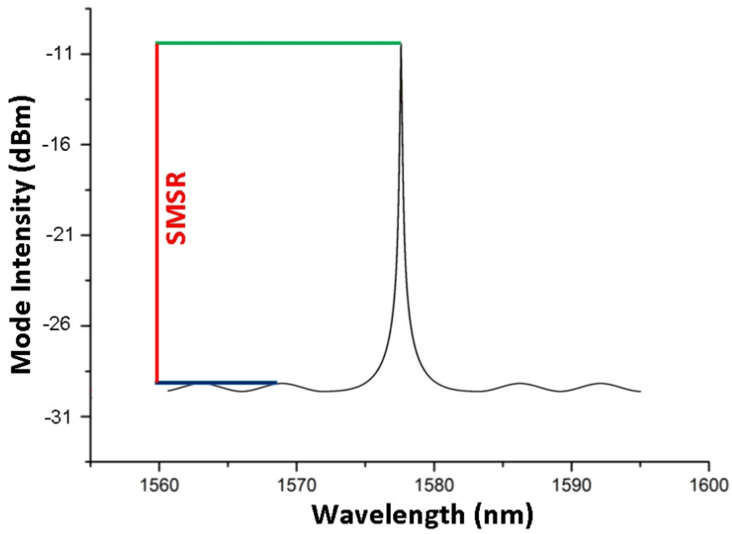

Fig. 6: An example of calculating SMSR in a system. The intensity levels of the main mode and the side mode are represented in green and blue, respectively, and their difference is denoted by the SMSR (red).

If Intensity$_{(\text{main mode})}$ and Intensity$_{(\text{side mode})}$ are the intensity levels of the main mode and side mode, respectively, mathematically, it can be expressed as

$$SMSR = \frac{Intensity_{(main\,mode)}}{Intensity_{(side\,mode)}}. \tag{3}$$

Since, in most cases, when characterizing lasers, the power is given in decibels (dB), the difference is

$$SMSR = Intensity_{(main\,mode)} - Intensity_{(side\,mode)}. \tag{4}$$

For this purpose, we identify the nearest side mode that exists for both FBGs separately, and then we investigate its influence when the system is operated in both modes. It was confirmed at the start of the experimentation that the side modes of both the main modes are present at their original locations [6, 24]. Repetitive experimentation yields some interesting outcomes that have been thoroughly discussed.

To attain the exact SMSR, we must subtract the displacement of mode x_1 from that of M_i, as ($x + x_1 - x_1 = x$). The same thing happens with M_o. When the value of the injection current increases beyond the threshold, all wavelengths undergo this experience, known as a red shift [18, 65].

Therefore, it is possible to explore the SMSR at that point. However, to determine the exact position of the side mode, the device calculating this position must be capable of finding the exact location of this mode before and after its relocation. Since both M_i and M_o are being analyzed, the side mode for M_i and M_o would also undergo displacement due to the red shift and might undergo another level of mode competition with the displaced wavelengths. Therefore, based on our understanding, it is possible with our current OSA (Optical Spectrum Analyzer AQ6375 [66]) to determine the displacement of the original modes and the side modes with high accuracy.

3. Overcoming Stability Challenges Due to Hysteresis in Passive Elements

In our experimental setup, an FBG serves as a crucial, passive sensing element. Over time, these FBGs have been employed extensively for various investigations, making them a central component of our research. However, given that an FBG is fundamentally a mechanical device, its performance can be subject to subtle changes related to material fatigue, stress relaxation, or environmental factors [46, 47]. These gradual alterations may introduce temporal variations in the FBG's output, potentially leading to discrepancies or drifts in measured values over extended periods. To address this potential source of error and ensure the long-term reliability and accuracy of our data, we undertook a comprehensive hysteresis analysis of each FBG individually. This analysis aims to characterize the relationship between the input stimulus (e.g., strain, temperature) and the FBG's output (e.g., Bragg wavelength shift) under cyclical loading conditions. By quantifying the hysteresis behavior, we can identify and potentially compensate for any non-ideal or time-dependent response characteristics. With the methodology employed for the hysteresis analysis of both FBGs, we present the results obtained and discuss the inherent challenges encountered during the process. This highlights the importance of understanding and mitigating these effects in long-term FBG-based sensing applications.

To ensure accurate and stable measurements of the Bragg wavelength, it is crucial to minimize heat losses and prevent temperature fluctuations. This can be achieved by implementing proper insulation and temperature control measures [48]. When the temperature is held constant, the Bragg wavelength remains stable over time, as depicted in Figures 7 and 8. This stability is essential for obtaining reliable and consistent measurement results. By avoiding detuning through temperature variations, we can maintain the integrity of our experiments and draw valid conclusions from their data.

(i) The SOA is attached to both gratings, one by one, with the injection current from 10 to 500 mA and constant temperature at 25°C. According to device specifications, the gratings require a stability time of 6-8 hours, which is observed to be approximately 10 hours in our case. This is related to the device's lifetime usage, which is a normal factor, especially for sensitive operations.

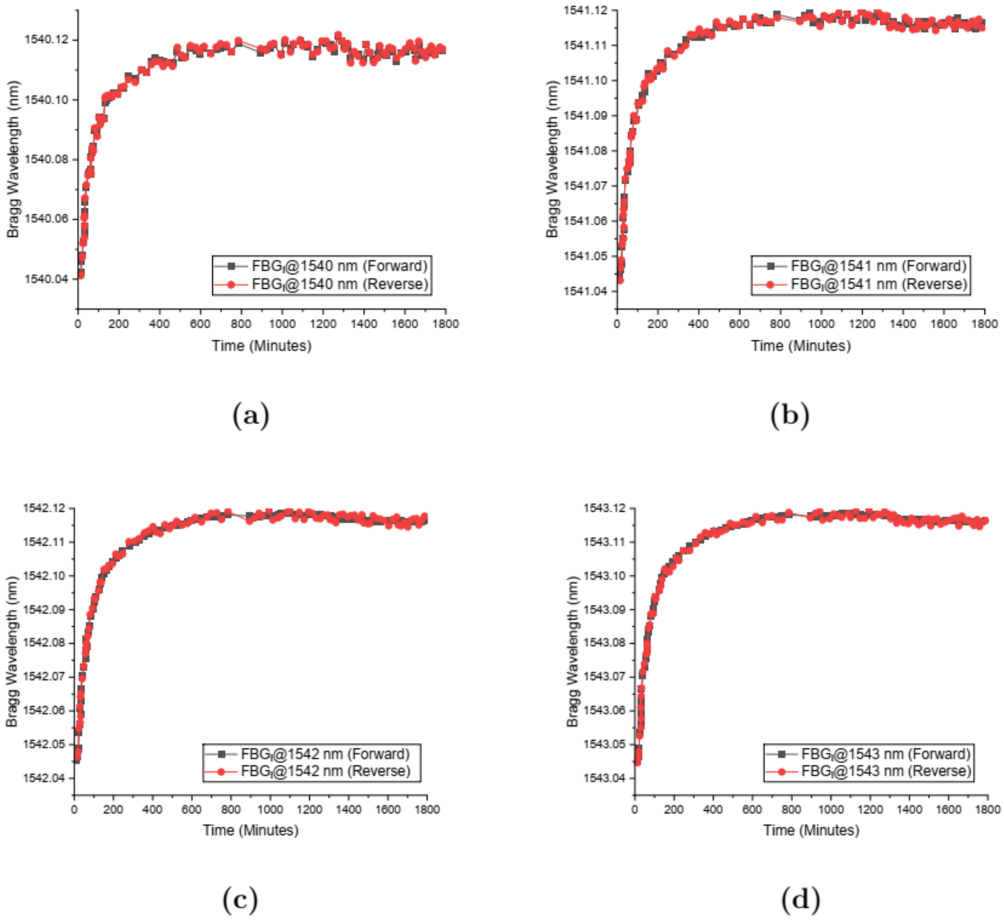

Fig. 7: Hysteresis analysis of FBG_i, at specified values of SOA temperature and injection current. The Bragg wavelength was set to (a) 1540 nm, (b) 1541 nm, (c) 1542 nm, and (d) 1543 nm, respectively.

(ii) The measurement of each FBG took about 1800 minutes at the specified SOA temperature and injection current, designated as the output in the forward direction. Afterwards, the current value was decreased from 500 to 10 mA, and the results were recorded in the reverse direction. The laboratory temperature during that time varied between 20.4°C and 24.7°C. Measurements were recorded every 5 minutes.

(iii) The procedure described above is followed for both the FBGs with their wavelengths set to 1540, 1541, 1542, and 1543 nm, respectively. The outcomes of both FBGs are provided in Figures 7 and 8.

(iv) From Figures 7(a), 7(b), 7(c), and 7(d), the value of Bragg wavelength is found to be within a range of ±0.08 nm for FBG_i. This holds true for the values in forward and reverse directions.

(v) Similarly, the Bragg wavelength is found to have a variation in the limit of ±0.08 nm for FBG_o, in Figures 8(a), 8(b), 8(c), and 8(d). This also holds true for the values in forward and reverse directions.

(vi) Obtaining a maximum difference in the Bragg wavelength of 3% from the targeted value during the hysteresis within the device's specifications is a significant achievement that highlights the sensitivity of the experimental setup.

(vii) The current system exhibits significant stability, emphasizing its practical application, with some limitations. Achieving the target wavelength requires an extended stabilization period exceeding 10 hours, after which only minor fluctuations in the Bragg wavelength are observed. This is clear from Figures 7 and 8.

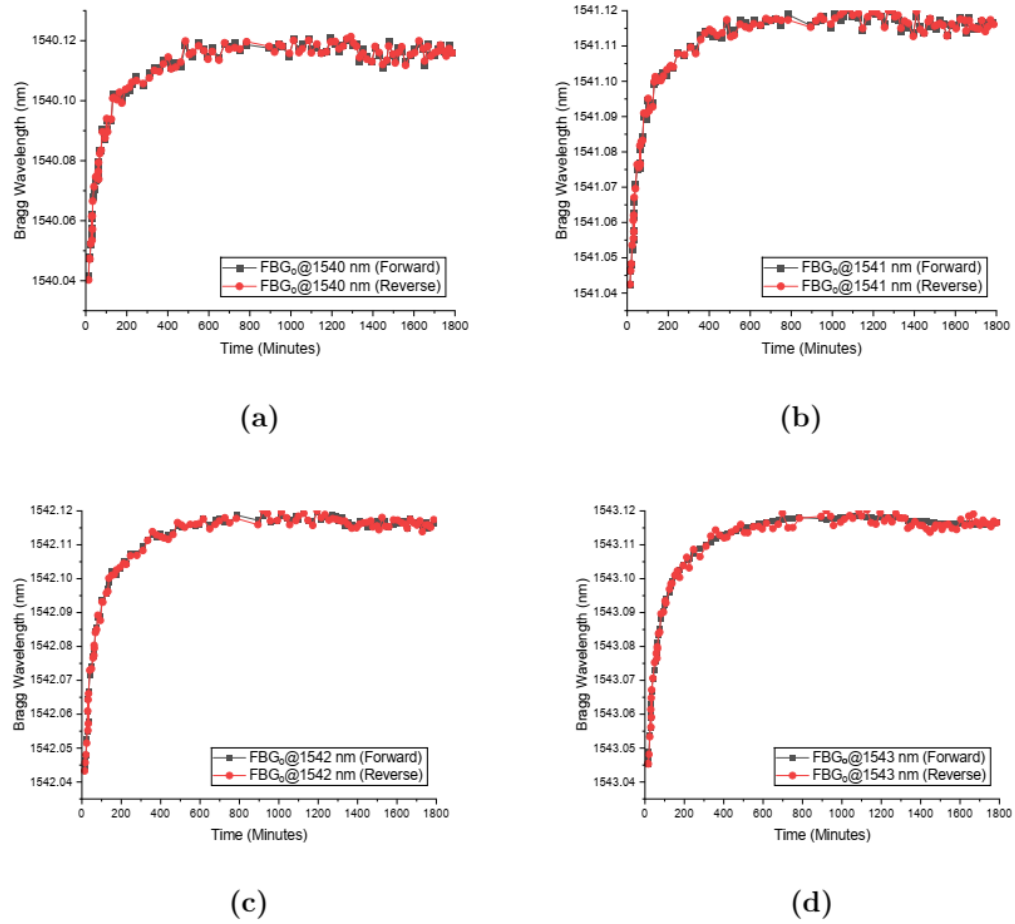

Fig. 8: Hysteresis analysis of FBG_o, at specified values of SOA temperature and injection current. The Bragg wavelength was set to (a) 1540 nm, (b) 1541 nm, (c) 1542 nm, and (d) 1543 nm, respectively.

(viii) A gradual wavelength increase occurs after 10 hours, likely attributed to the softening of the adhesive bonding the aluminium component to the FBGs due to thermal effects, leading to slippage. This long stabilization time presents a significant limitation, as immediate adjustments to mode spacing or position are not possible.

(ix) In view of the considerations above, a 24-hour waiting period is necessary before measurements can be considered stable, assuming minimal Bragg wavelength drift within a one-hour measurement window [67, 68]. Even then, long-term wavelength stability remains elusive, precluding dynamic spectral scanning via temperature-controlled wavelength adjustments due to insufficient precision.

(x) Furthermore, the current FBG's reflectance of only 99.2% limits resonator quality and consequently, the system's sensitivity. Achieving the desired sensitivity requires an improved resonator quality, necessitating FBGs with a reflectance of at least 99.99% [35, 49, 50, 52, 84].

The technical verdict of our investigation of both FBG_i and FBG_o is provided in Tables 2 and 3. We note that any fluctuations in the Bragg wavelength can have significant impacts on the performance of optical devices that rely on this wavelength for operation. Therefore, it is essential to prioritize care, respect, and truth in all measurements and experiments involving the Bragg wavelength beforehand.

TABLE 2. Determination of the Average Difference and Maximum Difference of Bragg Wavelength of FBG_i between the forward and reverse values, along with the stability time, after performing the hysteresis analysis at specific wavelengths in Figure 7.

No.	FBG_i Wavelength (nm)	Average Difference (nm)	Maximum Difference (nm)	Stability Time (Minutes)
1	1540	0.73	0.11	551
2	1541	0.65	0.11	538
3	1542	0.72	0.11	542
4	1543	0.64	0.11	547

TABLE 3. Determination of the Average Difference and Maximum Difference of Bragg Wavelength of FBG_o between the forward and reverse values, along with the stability time, after performing the hysteresis analysis at specific wavelengths in Figure 8.

No.	FBG_i Wavelength (nm)	Average Difference (nm)	Maximum Difference (nm)	Stability Time (Minutes)
1	1540	0.71	0.11	545
2	1541	0.67	0.11	534
3	1542	0.69	0.11	549
4	1543	0.71	0.11	556

4. Side Mode Suppression Ratio of the Dual Mode Experimental Setup

To determine the SMSR, the procedure is as explained in Section 2.f. The SMSR is specified separately for each laser line (in each mode). Figure 9 shows the SMSR obtained from the measurement setup in Figure 1(a) for both laser lines at SOA temperatures of 10°C, 15°C, 20°C, and 25°C. The SMSR of the laser line of FBG_i and FBG_o is shown in black and red, respectively.

The SMSR initially increases with each increase in temperature, as shown in Figure 9. The final value of approximately 50 dB achieved by the SMSR (sum of SMSR values for both modes) is almost identical across the examined temperatures, but it is achieved at different temperatures. At a temperature of 10°C, this nominal value is already reached at 295 mA. In contrast, at 15°C, 20°C, and 25°C, injection currents of 345 mA, 380 mA, and 425 mA are required, respectively.

4.a. Investigation of Mode Competition under Variation in Injection Current and Temperature on SMSR

The SMSR initially increases for all examined temperature values, as shown in Figure 9. This means that the value of SMSR depends explicitly on temperature, thereby determining the operation of the laser setup.

The final value of the SMSR achieved in these cases is almost identical at these temperatures; however, the point at which this value is reached is highly dependent on the specific temperature at which the measurement is performed. This aligns with recent work using tunable lasers [19, 32] conducted in a different wavelength range. Starting with the curve in Figure 9(a), it is seen that the values of SMSR for both modes increase gradually at a temperature of 10°C. The final value is reached at about 310 mA. Afterwards, the SMSR lies in the range of 22.5 and 26 dB. This means that both modes are dominant in this range of operation as compared to the side modes. This is a significant achievement for our laser setup.

It is observed that both modes maintain their values of SMSR within this specific range after the threshold current value is reached. According to medical consultations [72–74], this is very important because the Volatile Organic Compounds (VOCs), for which the laser sensor is designed, have specific characteristics that can only be observed under sensitive spectroscopic conditions. The modes must retain a certain intensity at a specific injection current and temperature [20].

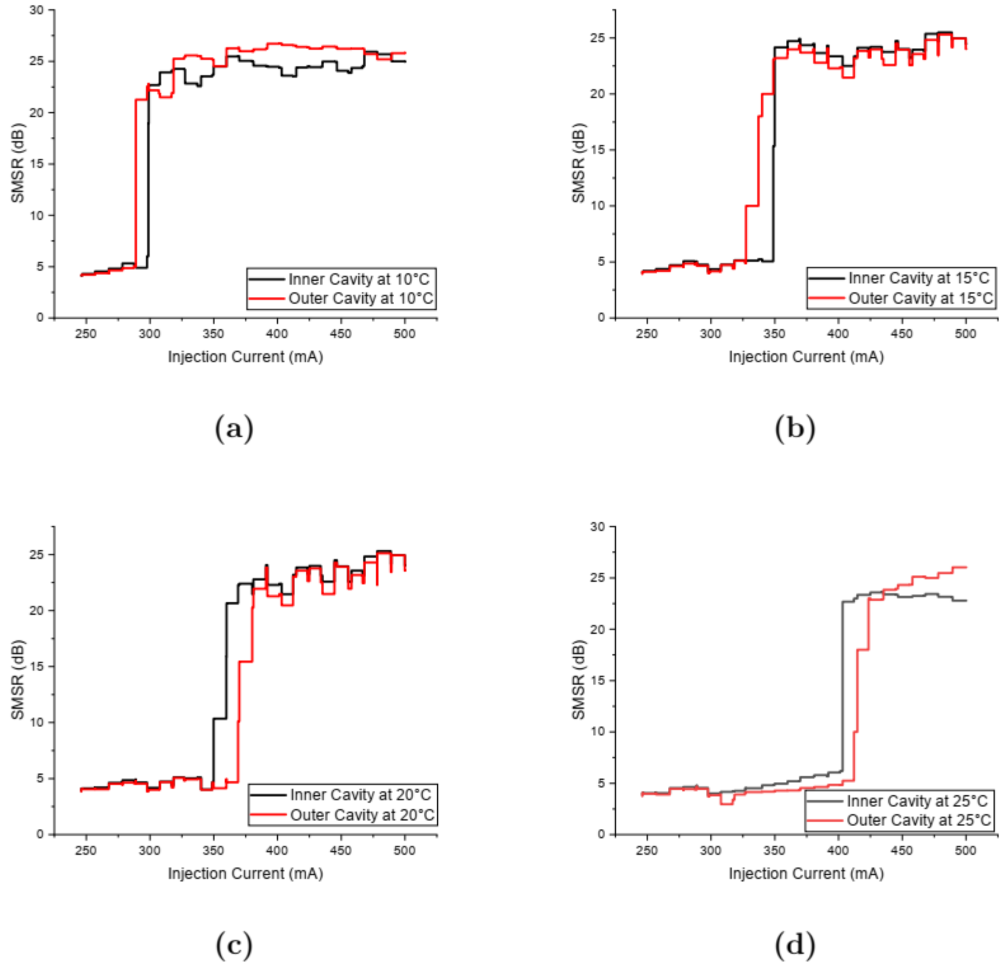

Fig. 9: Evaluation of the SMSR of both FBGs with increasing injection current, at various values of temperature (a) 10°C, (b) 15°C, (c) 20°C, and (d) 25°C, respectively.

Figure 9(a) shows that the inner mode attains a specific value of SMSR after the outer mode at 10°C. This means that Mo has less competition with the side modes as compared to M_i. There are numerous facts behind this phenomenon. First, the outer mode Mo (outer cavity) comprises FBG_o only, whereas the inner mode M_i (inner cavity) encompasses FBG_i as well as FBG_o. This means that SOA needs a specific value of injection current for FBG_o to cross the lasing threshold (outer cavity). In contrast, FBG_i requires additional effort to achieve the threshold current (inner cavity). Therefore, we expect M_o to be more stable in terms of intensity as compared to M_i. This is a consequence of cavity optomechanics that has been investigated for two specific wavelengths in this study.

At a temperature of 15°C, a similar trend has been observed for both modes in Figure 9(b). It is again seen here that M_o attempts to achieve SMSR at a threshold current of about 345 mA. Likewise, M_i achieves an SMSR value of approximately the same magnitude, which should be considered. An examination of this phenomenon reveals its connection to the quantum mechanical effects. As the temperature of a semiconductor material increases, the physical dimensions of the resonator also start to expand [21]. This phenomenon of thermal expansion significantly alters the spatial arrangement of the wavelengths (or modes) within the resonator. On this occasion, it is crucial to highlight and understand that these changes are intrinsically linked to the fundamental properties of the semiconductor crystal that is being used [22, 75].

When the temperature of the semiconductor rises, the increased thermal energy causes greater displacement between the atoms in its lattice. As a result, this thermal displacement leads to a reduction in the potential forces between the atoms. Consequently, the energy gap between the conduction and valence bands decreases in the semiconductor. A reduction in the bandgap energy results in an increase in the wavelengths of light that the semiconductor can interact with, leading to a corresponding shift in the refractive index of the material. This is evidence of red shift [18, 65, 76] and holds vital significance in technical terms [77, 78].

This shift in refractive index should be visualized because it implies that as the temperature rises, the wavelength of light within the semiconductor material experiences a red shift. Red shift refers to the phenomenon where the wavelength of light becomes longer as the energy of the photons producing this light decreases [79]. In other words, as the temperature increases, the wavelength of light that the semiconductor can effectively operate on during its operation becomes longer. The implications of this shift in wavelength are profound for the operation of semiconductor devices, particularly those that rely on precise optical measurements [80], such as the dual-mode laser system presented in this work. Here, we have observed the profound impact of this wavelength shift on the SMSR of the system, a crucial parameter. The change in redshift due to temperature changes can affect the performance and accuracy of these devices. As the resonator's function depends on specific wavelength ranges, it is clear that any change in these wavelengths directly impacts the device's functionality and efficiency. The value of the refractive index increases, which is caused by temperature-induced bandgap narrowing and can, therefore, lead to alterations in the resonator's operational characteristics.

To summarize this discussion, the relationship between temperature and wavelength shift in semiconductor materials is rooted in the principles of quantum mechanical effects [81]. As the temperature rises, the corresponding change in atomic displacement and potential forces within the crystal lattice results in a reduction of bandgap energy, leading to an increased wavelength of light and a higher value of refractive index. This phenomenon of redshift has significant consequences for properties of our dual-mode semiconductor device, such as SMSRs, affecting the performance and the accuracy of optical measurements.

Experimentation at 20°C yields a similar outcome. Here, we observe another interesting phenomenon: M_i achieves its SMSR at a current of approximately 370 mA, whereas Mo achieves it at approximately 385 mA. This means that the inner cavity now attains its SMSR quite before the outer cavity, which seems interesting. However, a closer examination of the matter reveals the primary reason behind it. When there are more electrons in the energy band as a result of more input current, they tend to occupy states that are very far from the edge. Therefore, we see transitions within that bandgap (Fermi level band filling [82]), in addition to the outer ones. This means that more energy is required to move the electrons from one point to another, causing a reduction in the corresponding wavelength, a phenomenon termed as blue shift. Thus, it is determined that the inner cavity achieves its SMSR before the outer one because of this phenomenon.

A key difference between the two temperatures shown is that at 20°C, the SMSR continues to increase after the threshold current is exceeded for both the outer cavity and the inner cavity. At 10°C and 15°C, the values of SMSR for both cavities remain within a relatively constant range. This is because an increase in the injection current, as per characterization of the SOA's datasheet [37], influences the maximum of the gain profile of the SOA. Therefore, increasing the injection current changes the relative position of the set wavelengths in relation to the gain maximum.

Another consequence of increasing the temperature to 25°C is that the SMSR of the inner and outer cavities is achieved at approximately 405 mA and 420 mA, respectively. The reason for this is the same as mentioned in the points above. However, here we see that the SMSR of the outer cavity increases afterwards, whereas that of the inner cavity starts to decrease. This may be related to the minute changes in rotational and vibrational spectra [34, 35]. However, an exact reason for this cannot be stated at this level.

The SMSR in all graphs indicates that both modes exist satisfactorily above the threshold current at all temperature values. This is essential for the laser system to be used as a spectroscopic sensor at a later stage, and is therefore, important to highlight at this level the precision of our principle.

4.b. Correlation with the Measurement Equipment

In light of the analysis presented above, it is now imperative to investigate the existence of both modes at their corresponding wavelengths throughout the entire operation of the experimental system. For this purpose, the measurements were performed with the help of a Thorlabs OSA (Thorlabs OSA202 OSA [69]) in another laboratory, which also operates by measuring the optical power of light signals across different wavelengths. It is essential at this point to emphasize the principle of spectrum analyzers that have been utilized for measurement purposes [70, 71]. The key features that are of interest for our system's operation are reviewed here.

Light Input

The Yokogawa AQ6370 accepts optical signals via fibre-optic input or free-space connectors, with similar input options for compatibility with various testing setups. The Thorlabs OSA202 typically receives optical signals via a fibre-optic input (e.g., FC/PC or FC/APC connectors) or a free-space input.

Wavelength Dispersion

The Yokogawa AQ6370 utilizes a diffraction grating for light dispersion, but its monochromator is specifically engineered for high spectral resolution, enabling more precise measurements, particularly in dense wavelength division multiplexing (DWDM) or other high-density applications. Thorlabs OSA202 also uses a diffraction grating to separate the light into its wavelength components. The diffraction grating is designed to offer good spectral resolution for a wide range of measurements.

Detection

Yokogawa AQ6370 uses a photodiode-based detector array, but with more advanced signal processing techniques, it can provide higher accuracy and faster data processing. The AQ6370 also benefits from more robust calibration for better measurement fidelity over time. Thorlabs OSA202 detects the separated light through a photodiode array or other suitable detectors, converting optical signals into electrical signals for spectrum analysis.

Signal Processing

Yokogawa AQ6370 processes the signal with high-speed DSP (digital signal processing), producing a more precise and stable spectrum. The AQ6370 features advanced capabilities, including automatic wavelength calibration, noise reduction, and high-speed data processing, enabling real-time results. Thorlabs OSA202 also processes the electrical signal and generates the optical spectrum, typically displaying power vs. wavelength data with real-time measurement capabilities.

Wide Wavelength Range and Resolution

The Yokogawa AQ6370 has a broader wavelength range (350 nm to 1650 nm) and higher resolution. The AQ6370 is specifically designed for high-precision measurements, supporting resolutions as fine as 0.01 nm, making it ideal for intricate analysis, including the testing of optical components in dense systems such as DWDM. Thorlabs OSA202 offers a decent wavelength range, typically around 600 nm to 1700 nm, with good resolution for many standard optical communications applications.

Real-Time Measurements

The Yokogawa AQ6370 provides real-time measurements with superior speed and accuracy. It is optimized for high-performance environments where fast, accurate, and stable real-time analysis is crucial, particularly for high-speed communication systems and research applications. The Thorlabs OSA202 also provides real-time spectral measurements, with a focus on ease of use and quick analysis for general applications.

Wavelength Range

The Yokogawa AQ6370 covers a wider range (350 nm to 1650 nm) compared to the Thorlabs OSA202 (600 nm to 1700 nm).

4.c. Validating Intensity Profiles of Inner Mode

The same operational conditions were established prior to the start of the experiment, as outlined in Section 2.f. The value of the SOA injection current was increased for every set of measurements in which the SOA temperature was maintained at 10°C, 15°C, 20 °C, and 25°C, respectively.

The observed initial increase in SMSR with temperature demonstrates a clear temperature dependence, as shown in Figures 10(a), 10(b), 10(c), and 10(d). This temperature sensitivity directly impacts how the laser setup performs. The differences between the values of the inner mode at their respective values of injection current and temperature are also shown in all figures.

While the final SMSR converges to a similar value across the tested temperatures, the temperature has a significant impact on the speed at which this value is reached. This observation aligns with recent findings on tunable lasers operating in a different wavelength range [25, 33].

For the sake of illustration, we examine the case of the inner mode at 10°C. Based on the data presented in Figure 10(a), the SMSR for both experimental setups exhibits a gradual increase starting at 10°C, reaching its peak value around 310 mA for both OSAs. Subsequently, the SMSR stabilizes within a range of 22.5 to 26 dB. This indicates a clear dominance of the inner mode over the side modes within this operational range, a noteworthy result for our laser setup.

After the threshold current is reached, the inner mode maintains its SMSR values within this range, despite intense mode competition. This is evident from Figures 10(a), 10(b), 10(c), and 10(d). This stability is critical because, according to medical consultations [35, 84], the VOCs targeted by the intended laser sensor require sensitive spectroscopic conditions for accurate detection. As also highlighted in [6], maintaining a specific mode intensity at a given injection current and temperature is essential for proper sensor function.

The consistent presence of the inner mode above the threshold current across all temperatures, as demonstrated by SMSR measurements, is crucial for the intended application of this laser system as a spectroscopic sensor. This stable, dual-mode operation underscores the precision of our fundamental principle, warranting specific emphasis.

For the sake of clarity, the differences in intensity levels between the inner mode and the equipment are shown in Figures 11(a) and 11(b). It is clear that the maximum value of the difference between the two modes is less than about 0.75 dB in all cases.

4.d. Validating Intensity Profiles of Outer Mode

The experimentation yielded interesting results for the outer mode, under the same parametric conditions outlined in earlier Section 2.f. It is observed that the pattern of the outer mode's existence displays a somewhat similar trend, albeit with a different level of intensity, as seen in the outcomes for the inner mode. This is clear from Figures 12(a), 12(b), 12(c), and 12(d). An increase in temperature shows a strong correlation with intensity in all cases shown in Figures 12(a), 12(b), 12(c), and 12(d).

For the sake of consistency, we see the intensity of the outer mode at 10°C in Figure 12(a). The SMSR for the outer mode with the Thorlabs OSA is in the range of 22.58 and 25.96 dB once the threshold value of the injection current is attained. This means that the outer mode sustains a high value during intense mode competition. This intense value at the output mirrors the intense sensitivity of the anticipated sensor setup.

As with the case of the inner mode, after the threshold current is reached, the outer mode maintains its SMSR values within this range, despite intense mode competition. This is evident from Figures 12(a), 12(b), 12(c), and 12(d). For proper sensor function, this sensitivity and stability are of importance.

To clarify, the differences in intensity levels of the outer mode, measured with both equipment setups, are illustrated in Figures 13(a) and 13(b). These figures demonstrate that the maximum difference between the mode intensities is less than approximately 0.75 dB in all scenarios.

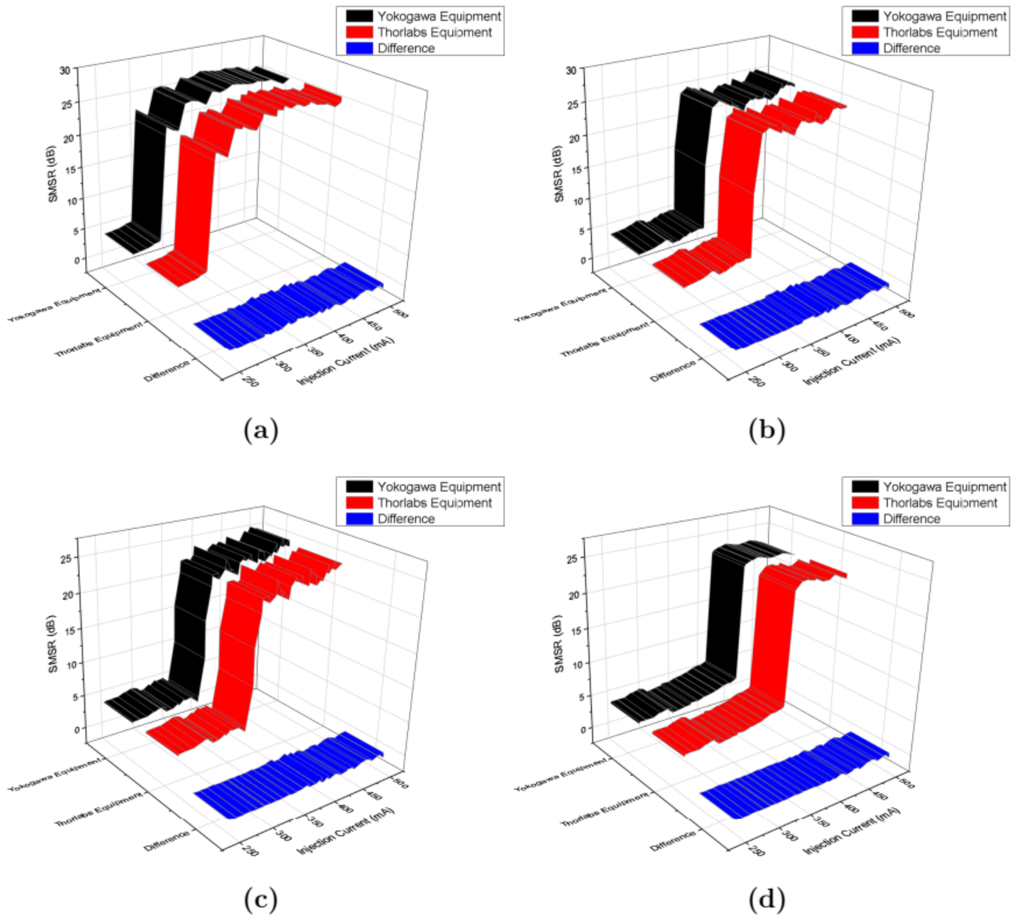

Figure 10: Comparison between the SMSR values of the inner mode M_i for experimental systems with Yokogawa OSA and Thorlabs OSA, with increasing injection current, at various values of temperature of (a) 10°C, (b) 15°C, (c) 20°C, and (d) 25°C, respectively.

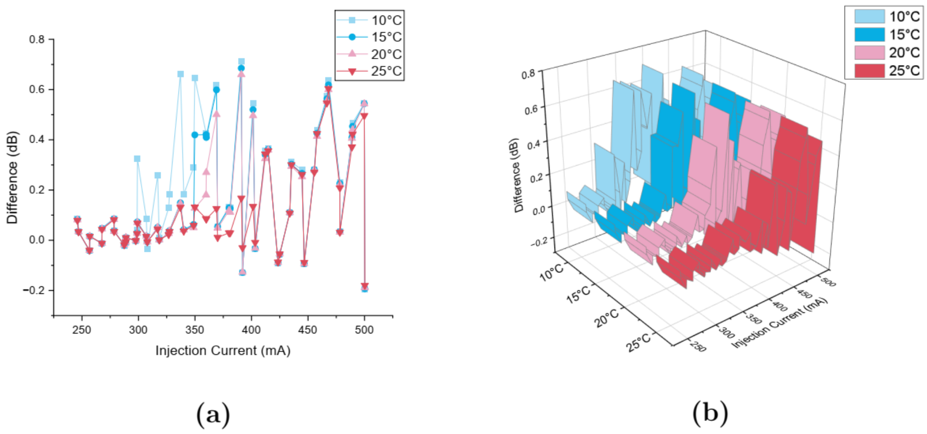

Fig. 11: Comparison of differences between the SMSR values of the inner mode M_i shown above in Figure 10(a) (corresponding to 10°C), Figure 10(b) (corresponding to 15°C), Figure 10(c) (corresponding to 20°C), and Figure 10(d) (corresponding to 25°C), in (a) 2D, and (b) 3D, respectively.

4.e. Illustration of Both Modes

Based on Figure 12(a), M_o reaches a specific SMSR at 10°C before M_i. This suggests that M_o experiences less competition from side modes compared to M_i. Several factors contribute to this behavior. The outer mode, generated by the outer cavity, is solely defined by FBG_o. In contrast, the inner mode, originating from the inner cavity, is influenced by both FBG_i and FBG_o. Consequently, the SOA requires a certain injection current for FBG_o to reach its lasing threshold (outer cavity), while FBG_i requires additional current to reach its own threshold (inner cavity). We therefore anticipate M_o to exhibit greater intensity stability compared to M_i, a result stemming from the cavity optomechanics investigated here for two specific wavelengths.

At 15°C, both modes shown in Figure 12(b) exhibit comparable behavior: Mo reaches SMSR at a threshold current of approximately 345 mA, a value similar to that observed for M_i. This consistency merits further consideration. This behavior appears to be related to quantum mechanical effects and the thermal expansion of the resonator at higher temperatures [21]. The resulting alteration of the wavelength or mode arrangement within the resonator is directly tied to the fundamental properties of the semiconductor crystal itself [22, 75]. As discussed earlier, this is a consequence of the red shift.

At 20°C, experiments yielded comparable results for both devices, revealing an intriguing phenomenon: M_i reaches its SMSR at approximately 370 mA, while M_o achieves its SMSR around 385 mA. This indicates that the inner cavity reaches its SMSR before the outer cavity, a consequence of blue shift, as noted earlier.

The behavior of SMSR with respect to injection current varies significantly across the tested temperatures for both experimental systems. At 20°C, the SMSR for both the inner and outer cavities continues to rise beyond the threshold current. However, at 10°C and 15°C, the SMSR values for both cavities remain relatively constant at a certain level. This difference stems from the effect of injection current on the SOA gain profile, as detailed in [37]. Higher injection currents shift the peak of the SOA gain profile, thus altering the relationship between the set wavelengths and the gain maximum.

At 25°C, the SMSRs of the inner and outer cavities reach their maximum values at approximately 405 mA and 420 mA, respectively, following the trend described previously. Post-peak, the SMSR of the outer cavity increases further, while the inner cavity's SMSR unexpectedly decreases. While subtle variations in rotational and vibrational spectra [34, 35] may contribute to this divergence, a definitive explanation requires further investigation.

To understand the difference between the intensity levels of the modes, it is essential to acknowledge their existence and the measurement protocols used. Both modes exhibit intense competition at various values of SOA injection current and temperature. This can be measured to a certain extent with the help of the OSAs. To accurately measure the fluctuations in intensity of the inner and outer modes in comparison to the side modes, the measurement equipment must be sensitive enough to yield a reasonable result.

As both Yokogawa and Thorlabs OSAs operate within the frequency range, the former provides an accuracy in wavelength of ±0.04 nm, from 1520 to 1580 nm. However, this holds at an ambient temperature of 23.5°C [66]. Although the room temperature falls within this range, the SOA's input parameters are in the range of 10°C to 25°C, a range that differs somewhat from these values. This means that the light flowing inside the experimental setup does not strictly follow the temperature pattern which is specified by the manufacturer.

Additionally, an FBG has been in constant use over time for various types of investigation. As a mechanical device, this implies a slight adjustment in the FBG outcomes, which may lead to differences in values. For this purpose, we decided to perform a prior hysteresis analysis on outcomes of both the FBGs, one by one, and have presented them in Figures 7 and 8, with an in-depth discussion in Section 3. Another reason that may restrict our results for the SMSR of both modes is the construction of the measurement devices [66, 69].

The Yokogawa OSA is based on the principle of a Michelson Interferometer. Here, the light is split into two beams, with one beam undergoing a variable optical path length change, while the other serves as a reference. These beams are recombined, creating an interference pattern that is analyzed to determine the wavelength components of the incoming light. This is the working principle of a Michelson interferometer, which is commonly used in spectrometers for high-resolution wavelength measurement and has a level of accuracy of approximately ±0.4 dB under specific device settings. The same is true for Thorlabs OSA, which operates on the principle of the Michelson Interferometer, and, beyond the presented results, restricts our outcomes under intense mode competition, especially at the threshold scenario [70, 71].

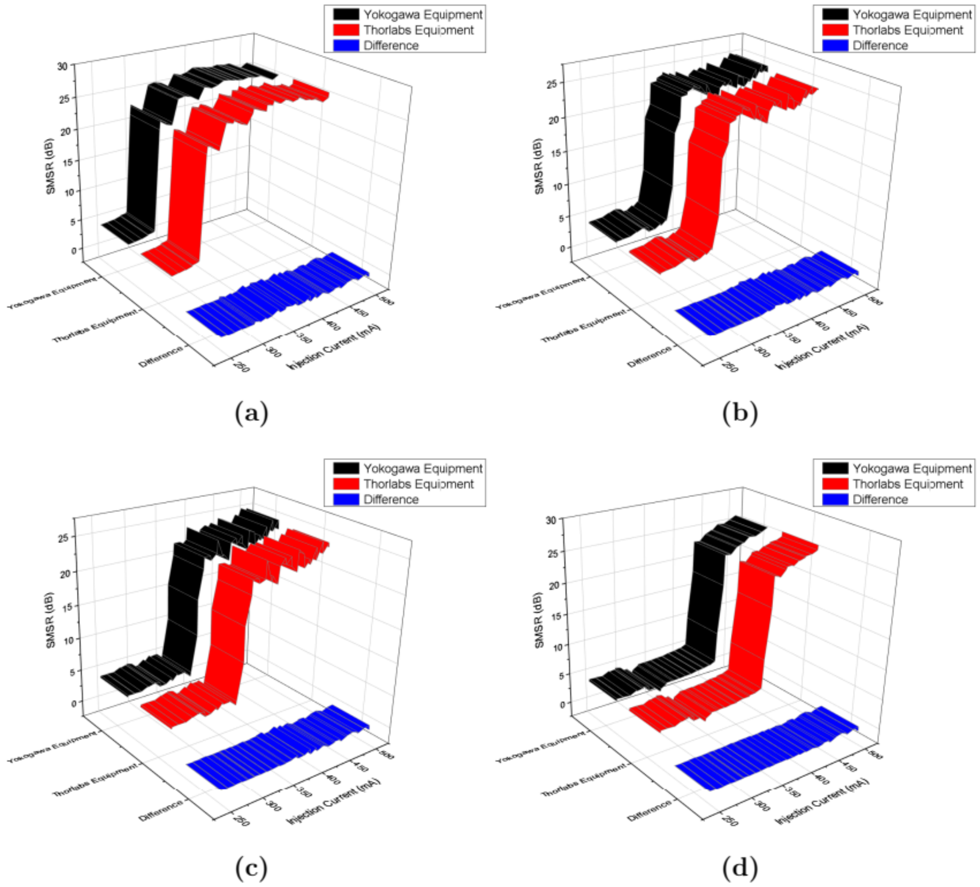

Fig. 12: Comparison between the SMSR values of the outer mode Mo for experimental systems with Yokogawa OSA and Thorlabs OSA, with increasing injection current, at various values of temperature of (a) 10°C, (b) 15°C, (c) 20°C, and (d) 25°C, respectively.

4.f. Discussion and Interpretation of Results

To illustrate these trends, the SMSR for selected injection currents at all examined temperatures is shown in Figure 14.

When the SOA is supplied with 350 mA of injection current, the SMSR of both FBG_i and FBG_o remains constant, respectively, at the start (Figure 14(a)). After 15°C, the SMSR of both modes decreases. A thorough analysis of this phenomenon again leads to the identification of quantum mechanical effects [36, 83, 84].

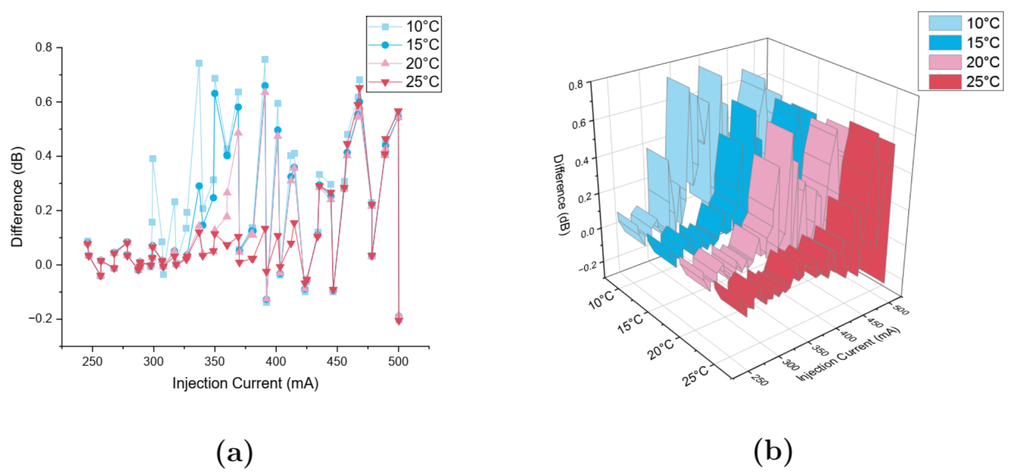

Fig. 13: Comparison of differences between the SMSR values of the inner mode M_i shown above in Figure 12(a) (corresponding to 10°C), Figure 12(b) (corresponding to 15°C), Figure 12(c) (corresponding to 20°C), and Figure 12(d) (corresponding to 25°C), in (a) 2D, and (b) 3D, respectively.

As the temperature increases, the semiconductor crystal expands, and its physical dimensions begin to increase. This, in turn, increases the length of the cavity in which this phenomenon takes place. This means that a mode (wavelength) that had been resonating earlier at a specified point changes its location. A mode that previously existed at a wavelength of x, now attains a wavelength $x + x_1$. Following this principle of expansion of the semiconductor crystal, all the modes that lie in this wavelength range move to higher values. Because of this phenomenon, the modes generated via FBG_i and FBG_o would also be displaced. The value of this displacement strictly relies on the properties of the semiconductor, which is InGaAs in our case.

As the average distance between the atoms inside the cavity increases, their electrostatic potential energy decreases. This explicitly lowers the band gap energy, thereby increasing the wavelength and the refractive index of the semiconductor. Therefore, the value of the wavelength reduces.

In the same figure, the SMSR drops for FBG_i earlier than that for FBG_o. One reason for this is the greater cavity length of FBG_i, as it encompasses FBG_o in it. When the temperature of the semiconductor remains below the threshold, a significant number of charge carriers (electrons) are present inside the energy band, because of which they tend to occupy those states that lie away from the band edge. As the Fermi energy level lies close to the valence band [82], we see transitions within the bands. As the temperature increases, free electrons and holes are generated, resulting in a corresponding shift of the Fermi level. Because of these intra-valence-band transitions, the energy increases, reducing the wavelength, a phenomenon commonly referred to as a blue shift [85, 86]. It is essential to comprehend this principle and its interplay within our system.

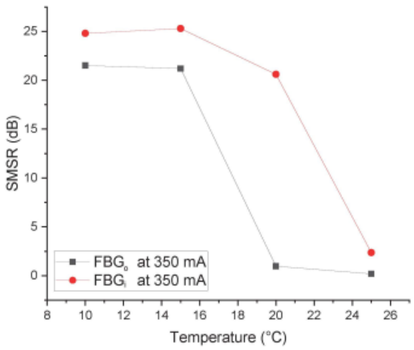

(a)

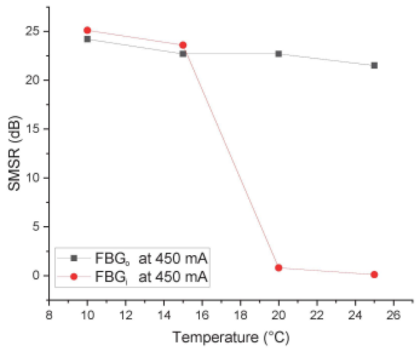

(b)

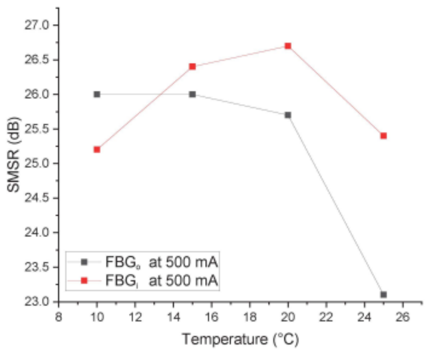

(c)

Figure 14: Comparison of the SMSR trends at various values of temperature, when both FBG_i and FBG_o are provided with an injection current of 350, 450, and 500 mA, respectively.

When two materials with differing Fermi levels are brought into contact with each other, a fundamental physical process occurs in which electrons migrate from the material with the higher Fermi level to the material with the lower Fermi level. This process of electron transfer continues until the Fermi levels of both materials reach an equilibrium. This means that the Fermi level of the material initially at a higher level decreases, whereas the Fermi level of the material initially at a lower level increases [87].

In this case, the Fermi level indicates the energy level at which the probability of an electron occupying a state is 50%. Thus, whenever two materials with different Fermi levels come into contact, this redistribution of electrons is a natural process driven by the tendency to achieve thermodynamic equilibrium in the lasing system.

For systems incorporating optical and electronic devices, such as those featuring FBGs and SOAs, the distinct material properties and corresponding Fermi levels present specific challenges. FBGs and SOAs are made from different semiconductor materials, and each of these materials has its own characteristic Fermi level [82, 88]. Once these materials have been integrated into a single system, the flow of electrons between them can result in intense mode competition. This can thereby affect the behavior of the optical modes at various temperatures and currents.

Such an interplay between semiconductor materials affects how they interact and function within the device. In other words, the differing Fermi levels can cause shifts in the operating characteristics of the devices under test, resulting in unusual behavior in the observed modes. This is exactly what we have noticed here. As a consequence, the performance of components like FBG_i, which intensely relies on this phenomenon within the system, drastically impacts the SMSR.

This impact holds extreme importance in the sense that achieving the maximum SMSR for FBG_i requires a higher energy input. This additional energy compensates for the mode competition and the shifts in mode behavior caused by the interactions between the FBG and the SOA. The graph illustrates that more energy is required to optimize the value of SMSR in FBG_i, demonstrating the practical implications of Fermi level adjustments and their effect on the operation of our dual-mode device. An understanding of these minute dynamics is crucial for fine-tuning our device's performance and ensuring an efficient operation in similar systems that involve multiple semiconductor materials.

At 450 mA, the SMSR of FBG_i drops in the same manner as in the earlier case above. This is because of the greater resonance area of its cavity. However, the SMSR of FBG_o remains between 25 and 22 dB. This is primarily because FBG_o has reduced cavity length at this value of SOA current, and a rise in temperature does not significantly influence the intensities of the side modes, despite their locations having altered. From a sensor's point of view, this means that the outcomes at this level are less affected by temperature, allowing the device to be used within this range for results with higher sensitivity. This is one of the desirable features of a medical device.

At 500mA, we see something interesting. The SMSR of FBG_o exhibits a drop similar to that of FBG_i in the previous case. First, this means that FBG_o is prone to temperature variation at higher values of SOA injection current. At this point, side modes start showing an increase in their intensity that somehow shuns the SMSR of FBG_o. A direct consequence of this mode competition is obvious from the SMSR trend of FBG_i. Here, the resonance length is greater than that of FBG_o, and the mode competition strikingly appears in the ranges from 10-15°C and 21-25°C. It is evident that the intensity of side modes increases; however, it is not possible to obtain more information about the side modes due to the aforementioned reasons, as outlined in the case of 15°C.

3. Conclusions

Our work involves a laser-based experimental setup designed for use in biomedical sensors. We attempt to use two wavelengths (modes) instead of one, due to the aforementioned reasons, which enhances the system's sensitivity. This significantly enhances the system's performance as an anticipated biomedical sensor, and mandates an intensive investigation of the FBGs. We start with precisely checking the splice points in the system. With FBGs being one of the core passive components in the system, a rigorous and successful hysteresis analysis of both these passive devices is performed, yielding a maximum difference of 0.11 nm and a stability time of 10 hours for all cases.

This is succeeded by a painstaking investigation of SMSR. An intense mode competition is revealed after analyzing SMSR at various values of injection current and temperature. The final value of SMSR is found to be almost identical across all temperature values, providing a mandatory validation of the idea behind using two wavelengths in the laser setup for a biomedical system. This means that the sensor principle can accurately detect and provide information about the amount of substances in the respiratory breath within the specified operating range. The inner mode experiences intense mode competition compared to the outer one, particularly at higher temperatures and currents, in correlation with cavity optomechanics and quantum mechanical effects in our experimental setup. M_i attains its respective SMSR after M_o at lower temperatures (10°C and 15°C), whereas we experience the opposite at 20°C and 25°C, thereby mirroring the technical role-play of red shift and blue shift in a dual-wavelength system. The entire experiment was thoroughly cross-checked with various measurement equipment, yielding an intensity difference of less than 0.75 dB for both M_i and M_o, which validates our findings. In this manner, the impact of temperature on these technical features of cavity optomechanics has been explored, playing a vital role in understanding and operating multiple modes in our system.

We have also examined the effects of temperature variation on the change in length of the dual-mode cavity, thereby providing valuable information about a significant change in the resonating wavelength of the InGaAs semiconductor. This helps uncover the phenomenon behind thermodynamic equilibrium in the given system. With an anticipated sensor in mind, the final value of the SMSR for both modes is expected to be stable, which has been satisfactorily demonstrated in this work through multiple investigations and supported by technical findings.

Funding

This research was funded by Princess Nourah bint Abdulrahman University Researchers Supporting Project number (PNURSP2025R19), Princess Nourah bint Abdulrahman University, Riyadh, Saudi Arabia.

Acknowledgements

This research was funded by Princess Nourah bint Abdulrahman University Researchers Supporting Project number (PNURSP2025R19), Princess Nourah bint Abdulrahman University, Riyadh, Saudi Arabia.

